Tandem Self-Powered Flexible Electrochromic Energy Supplier for Sustainable All-Day Operations

Jiaming Huang[1,2][†], Zhiwei Ren[1][†]*, Yaokang Zhang[3][†], Patrick Wai-Keung Fong[1], Hrisheekesh Thachoth Chandran[1], Qiong Liang[1], Kuanming Yao[4], Hua Tang[1], Hao Xia[1], Hengkai Zhang[1,2], Xinge Yu[4], Zijian Zheng[3]* and Gang Li[1, 2]*

Affiliations:

[1]Department of Electronic and Information Engineering, Research Institute for Smart Energy (RISE), The Hong Kong Polytechnic University, Hung Hom, Kowloon, Hong Kong, China.

[2]The Hong Kong Polytechnic University Shenzhen Research Institute, Shenzhen 518057, China.

[3]Laboratory for Advanced Interfacial Materials and Devices, Institute of Textiles and Clothing, Research Institute for Smart Energy (RISE), Research Institute for Intelligent Wearable Systems, The Hong Kong Polytechnic University, Hung Hom, Kowloon, Hong Kong, China.

[4]Department of Biomedical Engineering, City University of Hong Kong, Hong Kong, China

*Correspondence author. Email: zhiweipv.ren@polyu.edu.hk (Z.R.), zijian.zheng@polyu.edu.hk (Z.Z.), gang.w.li@polyu.edu.hk (G.L.)

[†] These authors contributed equally: Jiaming Huang, Zhiwei Ren, Yaokang Zhang.

Abstract

Self-powered wearable energy suppliers are highly desirable for next-generation smart electronic microsystems. However, it is still challenging to achieve an all-day operating self-powered energy device via the tandem integration strategy. Herein, we propose a tandem self-powered flexible energy supplier (SPFES) which 'harvest and store' energy from sunlight (outdoor), dim-light (indoor), and human body motion. In this novel device design, two flexible transparent electrodes are shared by three functional components: organic photovoltaic, triboelectric nanogenerator, and electrochromic supercapacitor. Interestingly, the SPFES shows distinctive in-built features including energy indication, self-modulation, and self-protection. When compared to mechanically stacked devices, the SPFES avoids unnecessary encapsulation and external connections, resulting in a thinner device with a higher power-to-weight ratio (up to 110 %). The concept of the SPFES paves an elegant route towards designing multi-functional flexible energy-harvest-storage devices for all-day operational wearable applications.

Introduction

The rise of the Internet of Things (IoT) demands miniaturized, wearable, and sustainable power suppliers for supporting smart electronics and health-monitoring devices.[1] The widely used flexible energy storage devices, for example, lithium-ion batteries (LIBs) and supercapacitors (SCs), have been regarded as powerful energy suppliers, but are unsustainable due to the periodical charging requirements.[2] Encouragingly, the emerging flexible energy harvesters show great potential for collecting energy from both environment and human body motion. Among them, organic photovoltaic (OPV) devices are promising for wearable electronics due to their superiorities in power-per-weight, flexibility, semi-transparency, and applicability in outdoor and indoor light conditions.[3] In addition, triboelectric nanogenerators (TENGs), which convert mechanical energy (*e.g.*, body motion) to electricity, have been regarded as state-of-the-art energy harvesters to drive miniaturized devices.[4] Nevertheless, due to the change in surroundings, these energy harvesters can hardly provide stable or regular energy directly to support smart electronics.[5] In this case, to realize a sustainable power supplier in wearable applications, integrating the complementary energy harvesters with energy storage devices is necessary.[4a, 4c, 6]

Self-powered flexible energy supplier (SPFES) that integrates energy harvesting and storage devices is a potential solution, although it currently faces numerous hurdles in its development. First, since the energy sources are intermittent, unpredictable, and are subjective to time, location, and behaviours of the wearer, current SPFES cannot fulfill the requirement of 24-7 indoor and outdoor operations.[7] For example, the operation of PV and TENG are respectively relying on light and motion. An ideal SPFES should harvest and store energy in multiple scenarios. Second, the current integrated SPFES is typically fabricated by mechanically stacking two or more independent devices. Thus, these devices possess redundant external terminals, unnecessary wire connections, and excessive plastic substrates, resulting in the fabrication complexity and increased device weight. Furthermore, energy efficiency and flexibility would be harmed,

3

resulting in a reduction in harvested energy per weight (power-per-weight). Designing a rational structure by intrinsically integrating multiple energy devices is essential for improving the power-per-weight and flexibility. Third, the currently reported multi-functional devices lack internal indications that reveal the energy-storage state in real-time.[8] These issues would impede the development of self-powered devices in wearable applications.
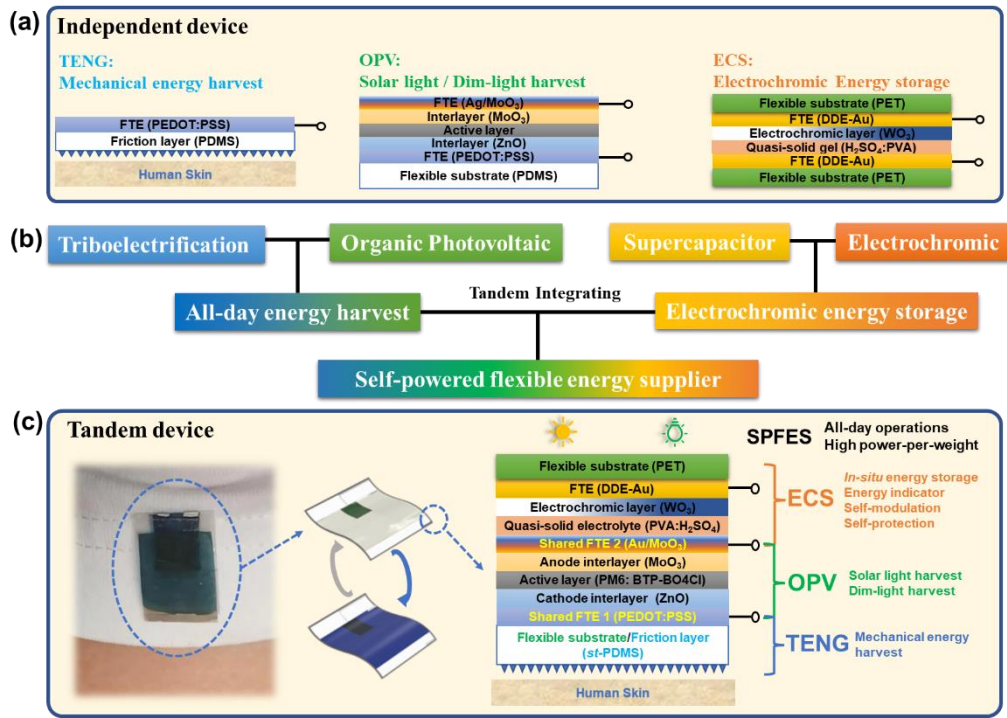
In this work, a tandem multi-functional SPFES is rationally constructed for the first time. The SPFES comprising the functions of OPV, TENG and electrochromic SC (ECS) can effectively 'harvest-storage' the outdoor solar energy, indoor dim-light energy, and mechanical energy in multiple scenarios. The energy storage status is dynamically indicated by the color variation from shallow grey (bleached state) to deep blue (full-charged state). In addition, the color-tunable feature of the ECS enables the SPFES with automatically tunable working modes (self-modulation) and prevents the OPV from unnecessary irradiation, thus elongating the operational lifetime (self-protection). Compared with the mechanical-stacking integration, the SPFES benefits from two critical interconnect flexible transparent electrodes (FTEs) showing reduced external terminals, and ~52% reduction in total thickness, resulting in excellent mechanical flexibility and durability. As a result, the SPFES shows a significant enhancement (up to 110%) in power-per-weight, compared with the mechanically stacked integrated device. Our work provides an elegant strategy to construct tandem multi-functional flexible electronics for future portable/wearable electronics.

Results

Design of the SPFES

To achieve a high degree of integration for OPV, TENG, and ECS, a tandem structure is rationally designed and is shown in Scheme 1. Figure S1 shows the detailed working principles of individual OPV, TENG, and ECS. In this structure, bottom and top FTEs of translucent OPV were shared with TENG and ECS, respectively. More specifically, fluoride surface-textured polydimethylsiloxane (*st*-PDMS) and high conductivity

PEDOT:PSS are shared by the OPV and the TENG. The *st*-PDMS/ PEDOT:PSS are employed as the friction layer and the FTE in TENG. Interestingly, the *st*-PDMS/PEDOT:PSS also serves as the intrinsic anti-reflection substrate and bottom FTE of flexible OPV.[9] Similarly, Au/MoO$_3$ was used as the top FTE of translucent OPV, which also serves as the FTE of ECS. Compared to the independent OPV, TENG, and ECS, our SPFES effectively reduce the fabrication complexity, with external terminals reduced from five to three (Scheme 1). More importantly, the thickness of the rationally designed compact SPFES is decreased to 200 μm when compared to the entire thickness of independent devices (>420 μm).

Scheme 1 a) Structure of free-standing OPV, TENG, and ECS; b) Diagram of the multi-function integration strategy of the SPFES; c) Photograph of SPFES (left), detailed materials and roles of all layers of the SPFES (right).

I. Outdoor (sunshine) and indoor (dim-light) energy harvesting: translucent flexible OPV

The n-i-p configuration of translucent flexible OPVs is *st*-PDMS@PEDOT:PSS /ZnO/Active layer/MoO$_3$/Au/MoO$_3$ (Figure 1a). Both the bottom and the top electrodes

are light-permeable, which promotes the OPV to harvest the light from both sides, making it highly suitable for multiple light source occasions.[10] Blended PM6 and BTP-BO4Cl function as the donor and acceptor materials in the active layer.[11] The chemical structures of the active materials and the absorption spectrum of the active layer are shown in Figure S2 and Figure S3, respectively. ZnO and MoO_3 are the corresponding electron and hole transport layers, respectively (Table S1, SI). The fabricating details are shown in SI. In this device, the *st*-PDMS@PEDOT:PSS and transparent Au (10-nm) /MoO_3 (240-nm) hybrid electrodes are the bottom cathode and the top anode, respectively.[12] The fabrication of the flexible *st*-PDMS@PEDOT:PSS electrode, which shows higher mechanical flexibility than other flexible substrates, is described in SI.[13] In brief, the *st*-PDMS was obtained by replicating the surface texture of a commercial 3M abrasive paper which was proposed in our previous work.[9] The surface textures of 3M papers and *st*-PDMS were measured by a 3D laser scanning microscope and scanning electron microscope (SEM) (Figure S4). Compared to the flexible substrate with a smooth surface, the micro-scale textures optimized the light absorption of the OPV by enhancing the diffuse transmittance (Figure S5a), decreasing the reflectance (Figure S5b), and introducing high haze (Figure S5c), which elongates the optical path to allow sufficient light absorption in the photoactive layer (Figure S5d) to increase the current density of the photovoltaic device.[9] Figure 1b shows the optical transmittance of the transparent electrode and the whole translucent OPV. Benefiting from the intrinsic anti-reflection substrate, the bottom FTE (*st*-PDMS@PEDOT:PSS) exhibits > 90% transmittance in the range of 400-650 nm, and > 80% high transmittance within the entire range of 300-1000 nm. On the other hand, the transparent top electrode (Au/MoO_3) shows >60% transmittance with a T_{max} of 82.1% at 512 nm. The average visible transmission (AVT) of the bottom and top electrodes from 380 nm to 780 nm is 91.51% and 69.43%, respectively (Equation 1, SI). The transmittance of the whole n-i-p device is also displayed in Figure 1b, demonstrating an AVT of 25.52% in the visible light range.

The photovoltaic performance of translucent OPV was measured under 1-Sun illumination (AM 1.5G) to simulate the outdoor conditions. The opaque device with a 100 nm-thick Ag electrode was fabricated and tested as a control device. The translucent device shows high power conversion efficiency (PCE) of 10.82% with an open-circuit voltage (V_{OC}) of 0.799 V, a short-circuit current density (J_{SC}) of 19.21 mA·cm^{-2} and a fill factor (FF) of 70.52% (Figure 1c and Table S2). The opaque device, on the other hand, has a greater J_{SC} because the opaque rear electrode acts as a reflector. When illuminated from the top side, the translucent device exhibits a V_{OC} of 0.775 V, a J_{SC} of 11.93 mA·cm^{-2}, and a FF of 71.76%, resulting in a PCE of 6.63%. The external quantum efficiency (EQE) spectra (Figure 1d) and the calculated current densities are in good agreement with the J-V curves.

Functioning under indoor dim light is another key feature of the OPV. In this scenario, the photovoltaic performance of OPV was measured under LED illumination (1000 lux, 2700K) to simulate the indoor lights. The input power and photon flux are shown in Figure S6a-c. The conversion relationship between input power and photon flux is explained in SI (Equation 2-4). The P_{in} of 1000 lux is calculated as 315.9 μW·cm^{-2} in this work. As shown in Figure 1e, the n-i-p opaque device shows a PCE of 17.00% with a reduced V_{OC} of 0.669 V, J_{SC} of 114.81 μA·cm^{-2}, and FF of 69.91%. The reduced V_{OC} is attributed to the low input power, according to the equation: $V_{OC} \propto \frac{nkT}{q} \ln P_{in}$.[14] The output power of the opaque OPV under 1000 lux LED illumination is 53.70 μW·cm^{-2}. The translucent OPV shows PCEs of 13.16% and 8.10% with the P_{out} of 41.56 and 25.59 μW·cm^{-2} when illuminated from the bottom and top sides, respectively. All the device parameters are summarized in Table S2.

To investigate the flexibility of the OPVs, the normalized efficiency of free-standing flexible OPVs was measured under repeated bending and twisting. After 1400 cycles of intense bending at a radius of 1.5 mm, 88.6% percent of the initial PCE is remained, as illustrated in Figure 1f. Meanwhile, the device retains 78.8% of initial PCE after 1000 times of irregular twisting. Corresponding st-PDMS@PH1000 shows an increase

in R_{sh} values by 1.24 and 1.41 times of pristine value. In conclusion, translucent OPVs exceptional mechanical stability and impressive PCE suggest that they have great potential for portable light harvesting under outdoor sunlight and indoor dim light.
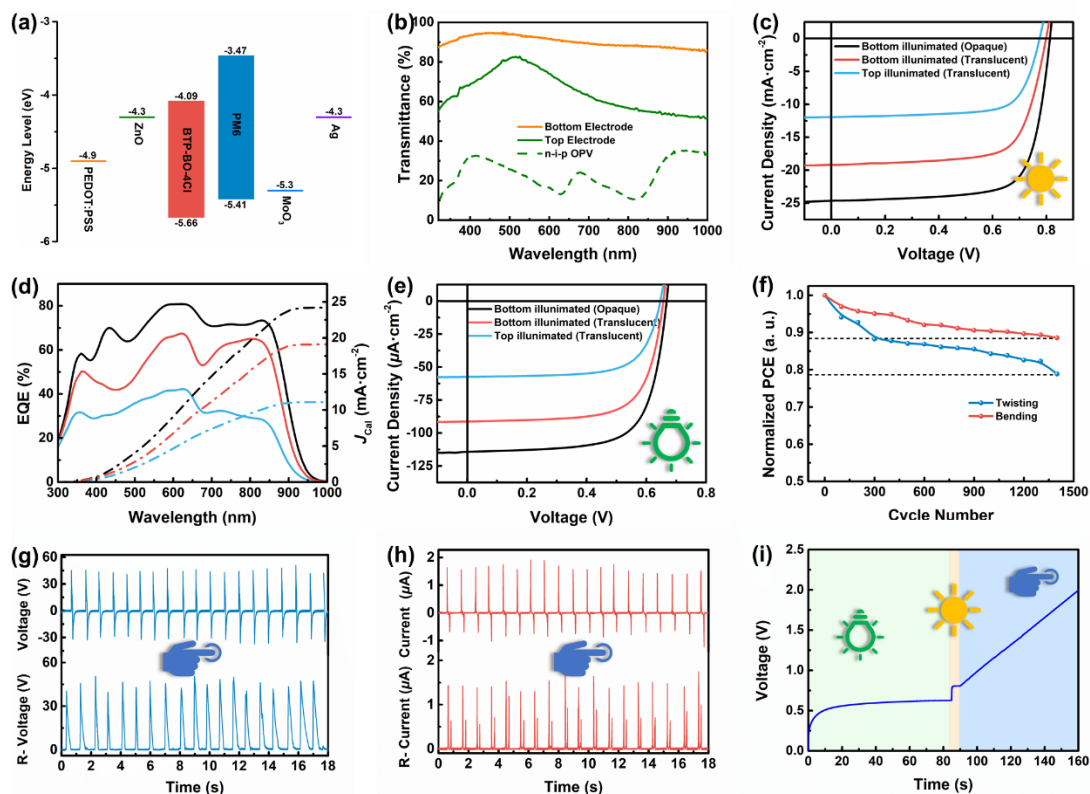

Figure 1 Characterization and performance of the hybrid energy harvest device. a) Energy alignment of OPV device with n-i-p configuration; b) Optical transmittance of transparent electrodes and the whole OPV; c) *J-V* curves under AM 1.5G spectra, d) EQE spectra; e) *J-V* curves under 1000lux white LED; f) Mechanical stability with continuous bending or twisting of OPV device with n-i-p configuration; g) Open-circuit voltage and rectified voltage, h) Short-circuit current and rectified current of TENG under continuous finger tapping; i) Dim light-charging (the green-shaded area), sunlight-charging (yellow-shaded area), and TENG-charging (blue-shaded area) to a 3.3 μF capacitor.

II. Mechanical energy harvesting: Single-electrode TENG

Rather than simple mechanical lamination, the TENG is intrinsically integrated with the OPV. The *st*-PDMS@PH1000 not only serves as the bottom electrode of the translucent OPV but also functions as the sharing electrode and the frictional layer of

the *s*-TENG. In brief, the periodical contact/separation between PEDOT:PSS and ground generate forward and reverse electron flows.[15] As shown in Figure 1g and Figure 1h, the V_{OC} and short-circuit current (I_{SC}) of the *s*-TENG under continuous finger tapping (1 Hz, 15 N) is ~ 45 V and 1.6 μA, respectively. The electrical performances of TENG were also measured at different frequencies and pressure forces (Figure S7). The TENG shows the improved output voltage and current with the increase in frequency and applied force, agreeing with the previous reports. [7b, 16] The *V* and *I* variation versus external load resistance was also measured (Figure S8). When the external resistance increases, the output voltage increases, and the output current decreases. Once the load resistance increases to 80 MΩ, the instantaneous output power reaches its maximum of 9.25 μW, and the instantaneous output power density is calculated as 4.63 μW·cm^{-2} (Equation 5-6, SI). Moreover, the average output power density of *s*-TENG is 367.5 nW·cm^{-2} (Equation 7-8, SI) and the effective output charge density (Equation 9, SI) is 9.27 nC·cm^{-2}. To evaluate the OPV/TENG hybrid energy harvesting device, the device is used to charge commercial capacitors.[15b] A full-wave bridge rectifier is employed to convert alternating current to direct current (Figure S9). The rectified voltage and current are shown in Figure 1g-h. The voltage profiles of different capacitors charged by TENG were also shown in Figure S10. When the S_1 switch is on, the capacitor is charged by the OPV under dim light and sunlight sequentially. The voltage increased to 0.56 V in 20 seconds under dim light conditions, as shown in Figure 1i, and then to 0.63 V (the green-shaded area). Once switched to sunlight, the voltage further increased to 0.8 V within 1.2 s (yellow-shaded area). The OPV charging process reaches saturation when the voltage of the capacitor almost equals the V_{OC} of the OPV. The capacitor can be further charged by the TENG when the S_2 switch is on. Under continuous tapping by a reciprocating motor, the voltage increases to 2 V in the next 70 s (blue-shaded area). The average charging power density of TENG is about 39.7 nW·cm^{-2} (Equation 10, SI). In this case, our OPV/TENG hybrid device can harvest light/mechanical energy in indoor, outdoor light, and the human body.

III. Chemical energy storage: ECS based on ultra-robust, flexible displacement-diffusion-etch Au (DDE-Au)

Electrochromic supercapacitor combines the functions of electrochromism and energy storage. In ECS, the energy storage level could be indicated by the reversible color change.[17] An ideal FTE of flexible ECS requires high conductivity and optical transmittance, strong adhesive force to the substrate, and long-term mechanical and chemical stability, especially for devices containing acid-electrolyte-like PVA:H_2SO_4.[18] However, state-of-the-art FTE can hardly meet these requirements simultaneously. Herein, DDE-Au coated (polyethylene terephthalate) PET reported in previous work was introduced as the transparent electrode of ECS.[19] The detailed fabrication process of DDE-Au was shown in SI. The DDE-Au/PET shows a transmittance over 80% at 550 nm (Figure 2a), and a low R_{sh} of 42.1 Ω/sq. Due to the strong binding between polymer and metal, the DDE-Au/PET demonstrates remarkable mechanical stability and a strong adhesiveness to the plastic substrate when using the solution-based polymer-assisted metal deposition (PAMD) technology.[20] The mechanical and chemical stability of DDE-Au FTEs is shown in Figure 2b-c. The DDE-Au show almost unchanged resistance under repeated bending at a radius of 2 mm. In comparison, the resistance of the commercial indium tin oxide (ITO)/PET increased over 20 times after bending under the same condition. It is worth noting that the resistance variation of DDE-Au is just 5% during each bending cycle, but the equivalent of ITO is about 10000 %. More importantly, the DDE-Au exhibits improved stability in a severely acidic environment (pH=1) for more than a month, outperforming commercial ITO/PET. To the best of our knowledge, solution-processed FTE with excellent robustness in such extremely harsh conditions has been never realized before. Because of the acid resistance and mechanical stability, high-performance flexible transparent supercapacitors with highly acidic electrolytes can be fabricated.

The electrochemical properties of DDE-Au and the quasi-solid-state ECS were investigated with a three-electrode cell system. Figure S11 shows the cyclic voltammetry (CV) and galvanostatic charging/discharging (GCD) of DDE-Au/WO_3 in

0.1M H_2SO_4 solution. The free-standing quasi-solid-state asymmetric (DDE-Au/WO_3(MoO_3)) ECS were also fabricated using PVA:H_2SO_4 as the electrolyte. The chemical reactions in ECS during charge and discharge are shown in SI. The enclosed shape is maintained under different scanning rates ranging from 25 to 200 mV·s^{-1}, indicating a good capacitive behaviour (Figure 2d and S9a). Figures 2e and S11b show GCD curves for current densities ranging from 0.125 to 2.0 mAcm^{-2} and voltages ranging from 0 to 0.8 V. All the areal capacitance (C_a) parameters are calculated from GCD curves (Equation 11, SI) and summarized in Figure 2f and Table S3. Under a current density of 0.125 mA cm^{-2}, the equivalent C_a for asymmetric ECS derived from the discharge curves is 21.19 mF cm^{-2}. In comparison, the DDE-Au FTE in 0.1M H_2SO_4 electrolyte shows C_a of 30.97 mF·cm^{-2} at 0.125 mA·cm^{-2}. The flexible DDE-Au-based ECS has one of the highest C_a values among flexible ECS.[17b, 21]
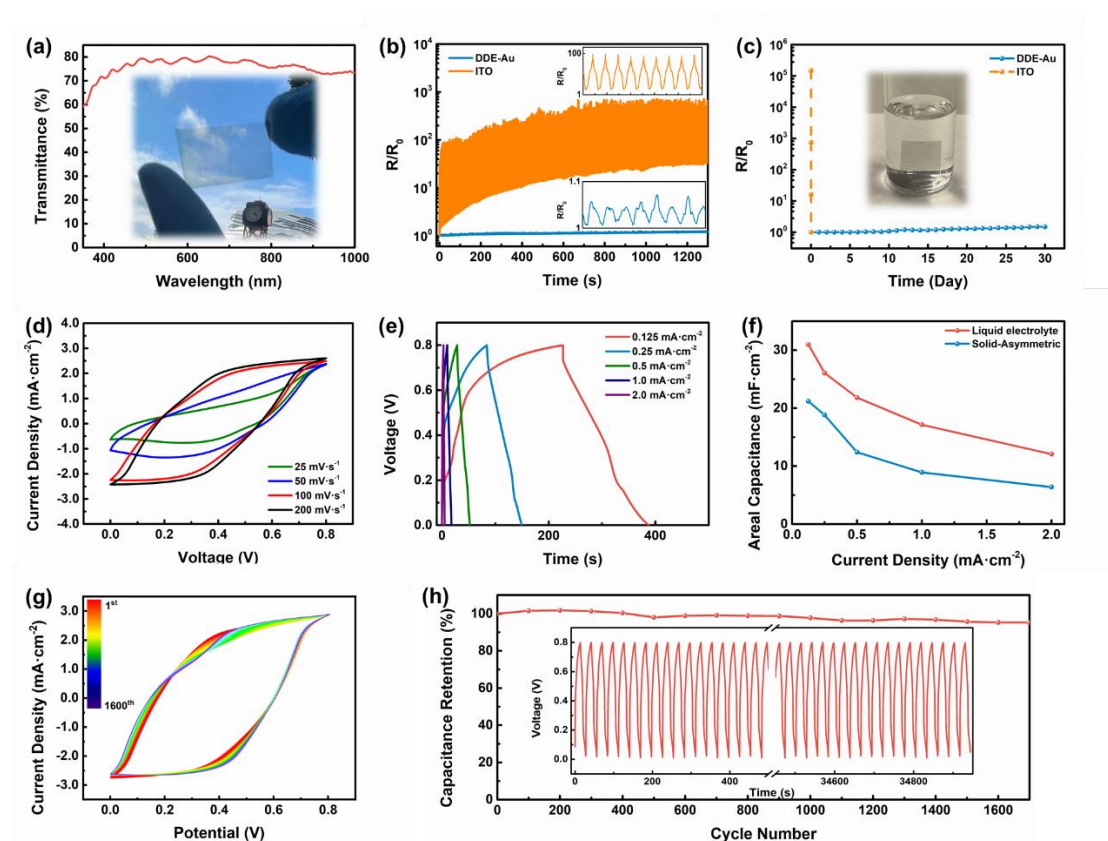

Figure 2 Characterization and performance of DDE-Au and corresponding ECS device. a) Optical transmittance of DDE-Au FTE. b) Mechanical stability of DDE-Au after continuous banding; c) Acid resistance test of DDE-Au FTE by immersing into 0.1 M H_2SO_4 over a month; CV (d) and GCD (e) of quasi-solid state asymmetric ECS; f) Summary of the areal capacitance of ECS based on liquid and quasi-solid electrolyte; g) CV of the ECS showing over 1600 consecutive cycles; h) GCD and calculated C_a of the ECS showing over 1600 consecutive cycles.

The ECS also shows a very high long-term cycling stability. Figure 2g displays the CV measurement of asymmetric ECS between 0 and 0.8 V over 1600 cycle times at 200 mVs^{-1}. The detailed CV plots at the 1st, 500th, 1000th, and 1600th cycles are extracted in Figure S12. After 1600 cycle times of ECS oxidation/reduction, a very stable current response was established with no discernible degradation or distortion. Meanwhile, the long-term GCD process was also investigated. Notably, according to the computed C_a in Figure 2h, after 1500 cycles, over 95% capacitance retention can be attained at a current density of 0.8 mA cm^{-2}. As a result, the DDE-Au-based ECS demonstrated greater stability during long-term charging and discharging.

The flexible ECS device based on DDE-Au shows a uniform color transition from light grey to deep blue. In contrast, the color transition of the ITO-based control device is not uniform (Figure S13), which is posited to the poor acid tolerance of ITO/PET. No obvious degradation or delamination of the DDE-Au/PET is observed after 0.1M H$_2$SO$_4$ immersion for 20 min, whereas the ITO is completely delaminated from plastic substrate within several minutes under the same condition (Figure S14).

IV. SPFES in multiple scenarios

The proposed SPFES harvest energy in a variety of settings, including outdoor, indoor, and sporting events. The fabricating details and cross-section diagrams of SPFES are shown in Figure S15. All the connections of tandem devices in working conditions are shown in Figure 3a. When the S$_1$ switch is on, the OPV could charge ECS under sunlight or dim-light conditions. While the S$_2$ switches on, the TENG could charge the ECS through the harvest of the mechanical energy in daily motion. During the charging process, electrons generated from OPV or TENG are injected into the ECS. Driven by the injected charge and the corresponding electric field, the electrons and the protons moved to the electrode accompanied by the protonation of WO$_3$. In this situation, the light and mechanical energy harvested by OPV and TENG are transformed into chemical energy, which is stored in ECS, with a color shift to indicate the charging condition.
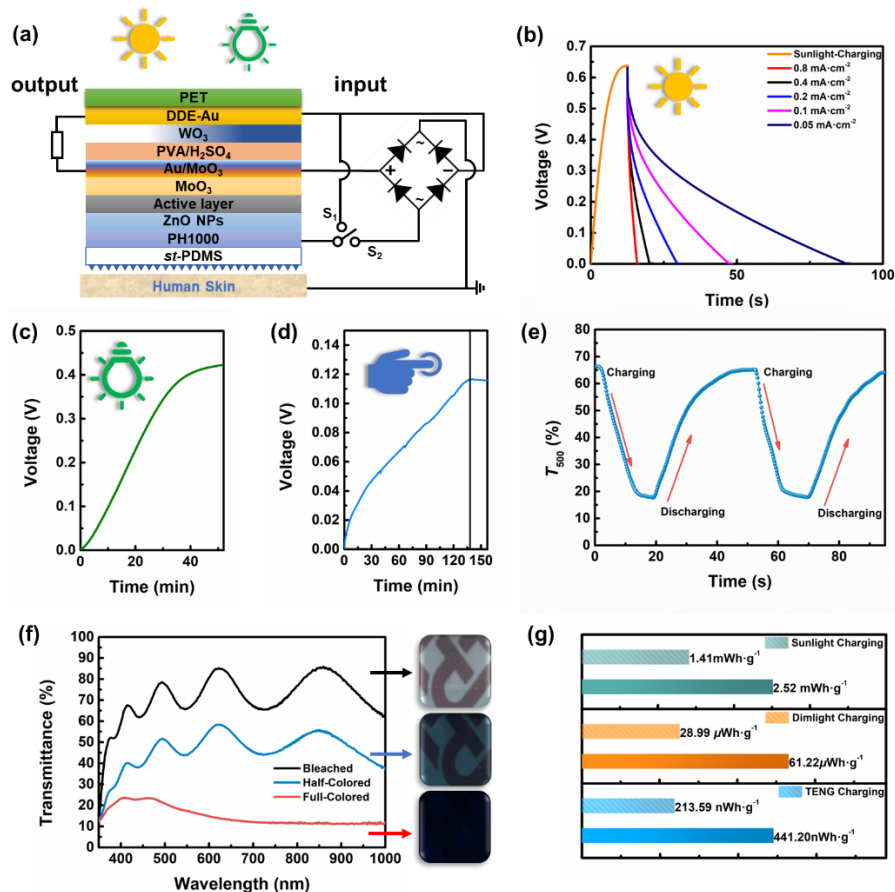
Figure 3 Characterization and performance of multi-functional SPFES. a) Device configuration and external connection of SPFES; b) The $V-t$ curves of sunlight charging and discharging process at different current densities; c) The $V-t$ curves of dim-light charging; d) The $V-t$ curves of TENG charging; e) *In-situ* variation of transmittance in 500 nm of SPFES under charging and discharging at 0.8 V; f) Optical transmittance and photographs of SPFES under different charging states; (inset) Photographs of SPFES under different colored states; g) Estimated harvest power-per-weight of (sparse pattern) the mechanical stacked device and (no pattern) SPFES for one day.

The charging processes are divided into three parts. (I): Sunlight charging; (II): Dim-light charging and (III): TENG charging. Figure 3b exhibits the photo-charging and discharging profiles under the 1-Sun condition of the tandem SPFES. The device is self-charged to 640 mV within 16 s. The color of the device starts to change when the voltage is increased to 480 mV (at 8 s). After that, the charging speed gradually slows down as the color deepens, until the voltage is close to the OPV's V_{OC} (full-charged state). The discharging process was conducted inside a shielded black box to avoid any extra charge input. According to the discharging curves, the calculated C_a (Table S4) is 3.73 to 2.94 mF·cm^{-2} under discharging current density ranging from 0.05 to 0.8 mA·cm^{-2} (Figure S16). The photo-charging process was also conducted under LED

13

illumination with an intensity of 1000 lux (Figure 3c). Due to the lower power of dim-light, the charging speed is much slower. The self-charging mechanism steadily increases the voltage to 100 mV in 500 seconds, eventually reaching a maximum of roughly 420 mV in 36 minutes. It indicates that the self-photo-charging behavior is feasible in both outdoor and indoor conditions. When the S2 switch is turned on, the TENG charging procedure begins.[22] According to Figure 3d, it takes roughly 130 min to charge the ECS to ~115 mV when a force of 15 N, 2.5 Hz is continuously applied. In this case, the SPFES simultaneously achieve the multifunction of *in-situ* energy harvesting and storage in multiple scenarios.

Accompanied by the charging and discharging behaviour, the SPFES exhibits automatically tunable optical transmittance with different energy storage levels.[23] Under a 0.8 V bias charge and discharge, the ECS's in-situ color response is measured (Figure 3e). In the charging process, optical transmittance decreases fast from 65% to 19% within 12 s and further reduces to 18% in the next 7.5 s. The bleaching response under reverse bias is relatively slower (30 s), which has been observed in other gel-based ECS.[24] Figure 3f shows the optical transmittance of SPFES under different charging states. The SPFES displays a high AVT of 71.20% under bleaching state, 46.17% under half-coloring state, and 14.96% under full-coloring state. The maximum transmittance values under coloring states are found at 400-500 nm, in the blue-purple area. Moreover, the above-illustrated color under different states is plotted on the CIE *xy* 1931 chromaticity diagram (Figure S17). The detailed parameters are summarized in Table S5. The central-located bleach state eventually transitions to the blue region with noticeable chromatic distortion as the charging process continues, which is consistent with the photograph. In simple terms, a shallow hue implies a low level of energy storage, whereas a deep color suggests a large level of energy storage. Such obvious chromatic aberrations endow SPFES with a smart function called energy indicator (Figure 4a).

The output power density of SPFES in the mode of sunlight-drive, dimlight-drive, and TENG-drive are 5.8-2.38 mW·cm^{-2}, 21.84-8.19 μW·cm^{-2} (under different charging states) and 367.5 nW·cm^{-2}, respectively (Table S6). The overall energy conversion and storage efficiency (η) is employed to describe the portion of the external energy (sunlight or dim-light) stored as electric energy in the ECS during the sunlight or dim-light charging. As calculated from Equation 12, the relationship of η versus time was provided in Figure S18.[24a] We have seen that the overall efficiency η gradually increases which means the energy has been starting to get stored in ECS. Then the η reaches the highest value of 1.64% (6.2 s) and 0.92% (35.6 min) during sunlight charging and dim-light charging, respectively. After that, despite the voltage of the ECS continuing to increase, the η gradually decreases. The overall efficiency decrease might be attributed to the light-blocking effect of the colored ECS, which makes the SPFES into the low-power mode. It would be illustrated in the following part (Part V).

To test the mechanical durability of the SPFES, continuous bending was applied. Figure 4b shows the photo-charging/discharging process under the 1-Sun condition of the SPFES and corresponding C_a after continuous bending cycles with a radius of 2 mm. The degradation in voltage is negligible, and the capacitance remained 80% of its initial value after 1600 cycles of bending. Moreover, two full-charged SPFES connected in series can easily enlighten four commercial red LEDs which demonstrate the basic usability of the SPFES (Figure S19).

As a comparison, mechanical stacked self-powered energy devices were also tested in this study (Figure S20-25, SI). Assuming that the SPFES works under the following scenarios: 1 sun for 1 h (sunlight charge), dim-light for 15 h (dim-light charge) and body motion for 8 h (TENG charge)[7a]. It is worth noting that the power-to-weight of SPFES, compared with the mechanical-stacked device, has been significantly improved up to ~78%, ~111% and 106% under sunlight mode, dim light mode and TENG charging mode, respectively (Figure 3g and Table S7). The enhanced power-to-weight of the SPFES is highly advantageous in wearable applications.

V. Self-modulation and self-protection

Generally, the energy harvesting devices should be turned off once the energy storage device is fully charged. Reducing the unnecessary working period of energy harvesting devices is a feasible way to elongate the service lifetime. Regular free-standing OPV usually suffers from reduced operational lifetime due to the long-time sunlight exposure. Hence, the key to optimizing the long-term benefits of self-powered gadgets is to manage the working and standby periods. Our proposed SPFES have such a smart self-modulation capability that can autonomously adjust the working mode based on the energy storage condition, which is encouraging (Figure 4c). Specifically, the incident light to OPV would be automatically modulated (blocked) by ECS. As a result, the SPFES exhibits three modes: high-power (bleached), low-power (half-colored), and standby (full-colored states). More importantly, the full-colored ECS would block most of the incident light and protects the OPV from unnecessary long-term light exposure. Such characteristics endow the SPFES with smart self-indicative, self-modulated, and self-protective features.

The *J-V* performance of SPFES was measured primarily under different charging states. The light sources (1-sun/dim-light) were illuminated from DDE-Au (top) side. Figure 4d-e shows the *J-V* curves of SPFES under 1-sun and dim-light conditions. Table S8 summarizes the detailed parameters. The J_{SC} decreases (high-power mode to low-power mode) as the charging process continues. A similar trend is observed under dim-light conditions. Under full-charged states, the SPFES show the PCE of 2.38% under sunlight, and 2.60% under dim-light conditions, respectively. Compared to the initial state, the SPFES is automatically tuned to the standby mode.

Moreover, the photostability test was conducted on free-standing OPV and full-charged SPFES under an LED array with equivalent 1 sun irradiation. Figure 4f shows the long-term light stability of free-standing n-i-p OPV and SPFES. The SPFES show 82.8% of initial PCE after 660 h illumination. In comparison, the free-standing n-i-p OPV shows an obvious PCE decay of 52.8% under the same condition. The detailed parameters are

16

shown in Figure S26 in SI. The free-standing device's significant degradation was primarily caused by V_{OC} and FF, indicating that the tandem device can substantially decrease the formation of defects by minimizing unnecessary light exposure during full-charged states. Such results show that our SPFES have the self-protective ability which can effectively elongate the operational lifetime of the photovoltaic effect of SPFES. The stability of the complete tandem device for 20 days was also tracked which is summarized in Figure S27.
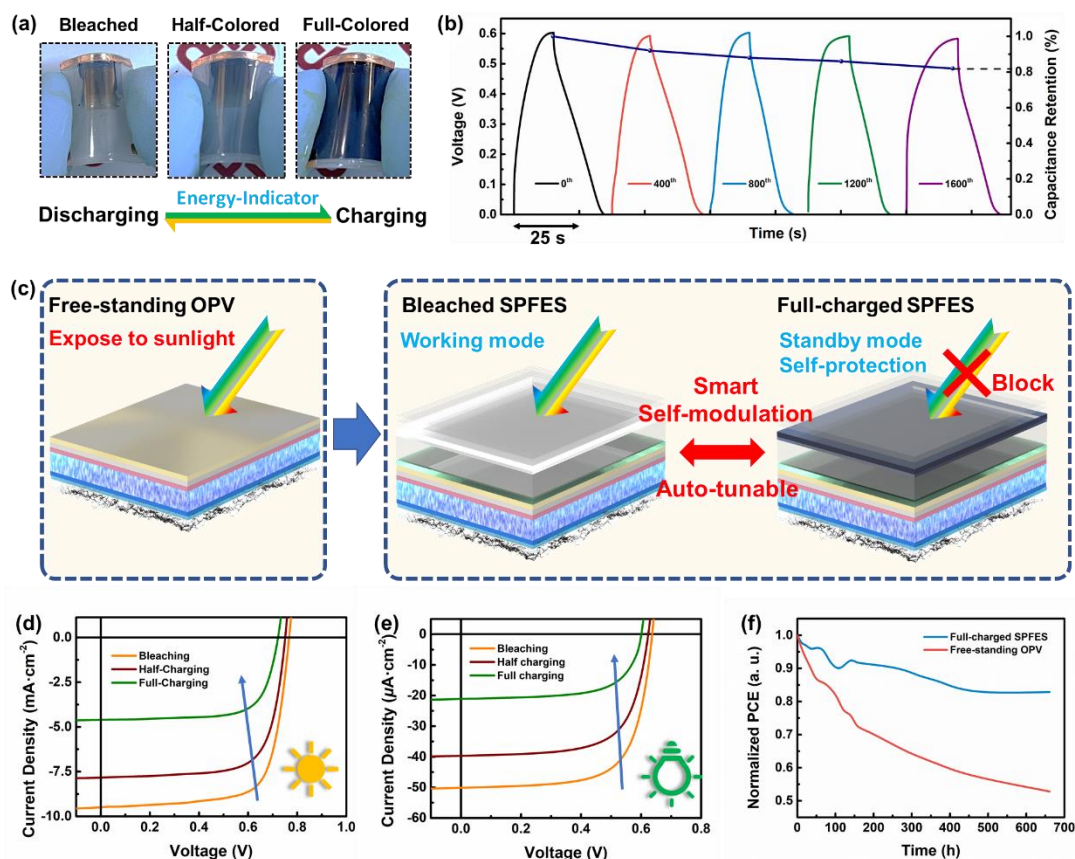

Figure 4 Distinct characters of SPFES. a) Self-energy-indicator: Photographs of SPFES under different charged states; b) mechanical stability of SPFES under continuous bending test; c) Schematic diagram of smart self-modulation and self-protection; d) *J-V* curves of SPFES under sunlight conditions; e) *J-V* curves of SPFES under dim-light condition; f) Normalized PCE of SPFES and free-standing OPV after light illumination.

Conclusion

In summary, we propose a multi-functional SPFES by rationally integrating ECS/OPV/TENG with shared FTE in the vertical direction. This tandem SPFES

effectively harvests energy originating from solar light (outdoor), dim-light (indoor), and mechanical movement (random body motion) in broad application scenarios. The harvested energy is further *in-situ* stored as chemical energy associated with color change for energy indication. Besides, the SPFES gives smart function capabilities like self-modulation and self-protection, which elongate the operational lifetime of the OPV unit in practical applications. More importantly, benefitting from the compact configuration, SPFES shows reduced external connections and device thickness which leads to excellent mechanical stability and durability. As a result, the SPFES exhibits over 70% - 110% higher power-per-weight compared to the mechanically stacked device with the same functions. Our work provides guidelines for constructing multi-functional self-powered devices, towards the practical applications in portable, wearable, and future smart window scenarios.

Materials and Methods
Materials
ITO glass was purchased from Zhuhai Kaivo Optoelectronic Technology Co. PEDOT: PSS Clevios PH1000 was purchased from Heraeus Clevis, German. PM6, BTP-BO-4Cl, were purchased from Solarmer Materials (Beijing) Inc and were used without any further purification. Other chemicals were purchased from Sigma Aldrich.

Fabrication of *st*-PDMS@PEDOT: PSS electrode (TENG device)
The PEDOT: PSS was first doped with 0.5% (v/v) Capstone™ FS-3100 and stirred for 30 min at room temperature. Then PEDOT: PSS (PH1000) was spin-coated onto silicon-wafer at 1600 rpm for 40 s and is followed by thermal annealing at 110 °C for 10 min. Formic acid was then dropped onto the pristine PEDOT: PSS (PH1000) for 10 min acid treatment. The residual acid was removed by thermal annealing at 110 °C for 10 min.

Dow Corning® SYLGARD PDMS 184 precursor and curing reagent were mixed with a ratio of 10:1(w/w) and degassed at vacuum chamber for 40 min. After that, the mixture was blade-coated onto the obtained PESOT: PSS film. Then, the sample was put into

an oven and cured at 80 °C for 10 min. The pre-cured PDMS was covered by 3M abrasive paper (mesh number: 6000) and followed by curing at 80 °C for 2h. The abrasive paper was peeled off first. The textured surface of PDMS was further treated with fluoro silane to reduce the surface energy. The cured PDMS@PEDOT:PSS FTE was peeled off from the wafer and laminated on a piece of glass for further use. The silver paste was used to improve the contact for further testing.

Fabrication of n-i-p OPV device

By using ZnO nanoparticles instead of sol-gel ZnO as the electron-transport layer, high-temperature processing (200 °C for 30 minutes) is avoided, which exceeds the tolerance of the PDMS@PEDOT: PSS. ZnO NP is diluted in IPA (1: 4) and ultrasonicated for 1 h. The ZnO NP is spin-coated on PH1000/PDMS with 3000 rpm for 40 s and thermally annealed at 100 °C for 10 min. The processing of the active layer is similar to the conventional device. 5-nm MoO_3 and 100-nm Ag were then vacuum deposited as the opaque electrode. For translucent devices, 10-nm Au and 240 nm MoO_3 were deposited sequentially. The effective area of solar cells is 0.09 cm^2.

Fabrication of DDE-Au electrode

1 wt% P(MBP-co-METAC) copolymer was dissolved in 2-methoxylethanol. The solution was spin-coated onto the PET at 3,000 rpm for 30 s, followed by thermal annealing at 120 °C for 5 min. The PET was cured under a UV lamp for 5 min. Afterward, the substrates were immersed in a 2 wt% solution of $(NH_4)_2PdCl_4$ for 1 min. Finally, the sample was rinsed with DI water, and then immersed in the Cu plating bath. The recipe for the Cu plating bath can be found in our previous publication.

The obtained PAMD Cu was immersed in 2.5 mM $HAuCl_4$ solution for 1 min and then rinsed with DI water. After drying with compressed air, the substrates were annealed at 150 °C for 10 min on a hotplate. As a final step, the substrates were immersed in 1 M $FeCl_3$ solution for 10 s to remove the residual Cu.

Fabrication of ECS

A 240-nm WO_3 was deposited onto the obtained DDE-Au electrode on PET by E-beam

evaporation. Poly(vinyl alcohol) (PVA) and 1 M H_2SO_4 were mixed with the weight ratio of 1:1 and stirred at 80 °C overnight until the mixture became clear. To remove the excess water, the combined gel was bladed on WO_3 and stored overnight at room temperature. Another DDE-Au electrode was then laminated onto the electrolyte to form a solid-state flexible ECS. For the asymmetric ECS, the obtained PET/DDE-Au/WO_3/electrolyte was laminated onto the MoO_3/Metal electrode to form a quasi-solid state flexible ECS.

Fabrication of tandem device

To balance the energy harvest and storage, 110-nm WO_3 was used in a tandem device. Other parameters are similar to the fabrication of ECS. The SPFES was fabricated by laminating the obtained PET/DDE-Au/WO_3/electrolyte to the n-i-p translucent OPV device.

Characterizations

Morphology of PDMS and abrasive paper were measured by a 3D laser scanning microscope (KEYENCE VK-X200) and SEM (Tescan VEGA3). Transmittance and absorption were measured by Varian Cary® 300 UV-Vis spectrophotometers (Agilent Technologies) with an integrating sphere. The sheet resistance was conducted by four-terminal measurement. The *J-V* curves were measured in the glovebox with a Keithley 2400 unit under 1 sun, AM 1.5G spectra (100 mW·cm^{-2}) from a solar simulator (Enli Tech. Co., Ltd., Taiwan). The light intensity was calibrated with a 20 mm × 20 mm monocrystalline silicon reference cell with a KG5 filter (Enli Tech. Co., Ltd., Taiwan). The EQE spectra were measured by QE-R3-011 (Enli Tech. Co., Ltd., Taiwan). The light intensity at each wavelength was calibrated with a standard single-crystal Si photovoltaic cell. The LED lamp was purchased from Philips (CorePro E27 LED GLS Bulb 8 W(60W), 2700K, Warm White, GLS shape). The light spectra were measured by the Ocean Optics spectrometer (QE65000). The mechanical stability (bending, twisting, and stretching) was performed in the glovebox without encapsulation. The OPV device used for the mechanical stability test is the translucent device with the

bottom illumination under AM 1.5G (100 mW·cm^{-2}). The CV and GCD measurements were conducted by Autolab PGSTAT302N. The open-circuit voltage (V_{OC}) and short-circuit current (I_{SC}) of TENG, as well as the photo-charging/discharging process, were measured using a semiconductor analyzer (Keysight B1500A). An electrometer (Keithley 6514) was used to measure the TENG-charging process.

Reference

[1]   a)M. Kaltenbrunner, T. Sekitani, J. Reeder, T. Yokota, K. Kuribara, T. Tokuhara, M. Drack, R. Schwodiauer, I. Graz, S. Bauer-Gogonea, S. Bauer, T. Someya, *Nature* **2013**, 499, 458; b)C. Wang, X. Li, H. Hu, L. Zhang, Z. Huang, M. Lin, Z. Zhang, Z. Yin, B. Huang, H. Gong, S. Bhaskaran, Y. Gu, M. Makihata, Y. Guo, Y. Lei, Y. Chen, C. Wang, Y. Li, T. Zhang, Z. Chen, A. P. Pisano, L. Zhang, Q. Zhou, S. Xu, *Nat. Biomed. Eng.* **2018**, 2, 687; c)X. Pu, W. Hu, Z. L. Wang, *Small* **2018**, 14, 1702817.
[2]   a)B. Chen, L. Xu, Z. Xie, W.-Y. Wong, *EcoMat* **2021**, 3, e12106; b)K. Naoi, W. Naoi, S. Aoyagi, J.-i. Miyamoto, T. Kamino, *Accounts Chem Res* **2013**, 46, 1075; c)W. Raza, F. Ali, N. Raza, Y. Luo, K.-H. Kim, J. Yang, S. Kumar, A. Mehmood, E. E. Kwon, *Nano Energy* **2018**, 52, 441.
[3]   a)P. Cheng, G. Li, X. Zhan, Y. Yang, *Nat. Photonics* **2018**, 12, 131; b)G. Li, W. H. Chang, Y. Yang, *Nature Reviews Materials* **2017**, 2, 17043; c)L. Meng, Y. Zhang, X. Wan, C. Li, X. Zhang, Y. Wang, X. Ke, Z. Xiao, L. Ding, R. Xia, H.-L. Yip, Y. Cao, Y. Chen, *Science* **2018**, 361, 5; d)G. Li, V. Shrotriya, J. Huang, Y. Yao, T. Moriarty, K. Emery, Y. Yang, *Nat. Mater.* **2005**, 4, 864; e)W. Song, K. Yu, E. Zhou, L. Xie, L. Hong, J. Ge, J. Zhang, X. Zhang, R. Peng, Z. Ge, *Adv. Funct. Mater* **2021**, 31, 2102694; f)C. Yan, R. Ma, G. Cai, T. Liu, J. Zhu, J. Wang, Y. Li, J. Huang, Z. Luo, Y. Xiao, X. Lu, T. Yang, X. Zhan, H. Yan, G. Li, *EcoMat* **2020**, 2, e12061; g)C. Yan, J. Yu, Y. Li, P. W. K. Fong, R. Ding, K. Liu, H. Xia, Z. Ren, X. Lu, J. Hao, G. Li, *Matter* **2022**, 10.1016/j.matt.2022.04.028.
[4]   a)F.-R. Fan, Z.-Q. Tian, Z. Lin Wang, *Nano Energy* **2012**, 1, 328; b)Z. L. Wang, J. Chen, L. Lin, *Energy Environ. Sci* **2015**, 8, 2250; c)Y. Zi, S. Niu, J. Wang, Z. Wen, W. Tang, Z. L. Wang, *Nat. Commun.* **2015**, 6, 8376; d)J. W. Lee, S. Jung, J. Jo, G. H. Han, D.-M. Lee, J. Oh, H. J. Hwang, D. Choi, S.-W. Kim, J. H. Lee, C. Yang, J. M. Baik, *Energy Environ. Sci* **2021**, 14, 1004; e)J. Luo, Z. L. Wang, *EcoMat* **2020**, 2, e12059.
[5]   a)Y. Yuan, Y. Lu, B. E. Jia, H. Tang, L. Chen, Y. J. Zeng, Y. Hou, Q. Zhang, Q. He, L. Jiao, J. Leng, Z. Ye, J. Lu, *Nanomicro Lett* **2019**, 11, 42; b)Z. Zhao, K. Xia, Y. Hou, Q. Zhang, Z. Ye, J. Lu, *Chem. Soc. Rev.* **2021**, 50, 12702.
[6]   a)Z. L. Wang, J. Chen, L. Lin, *Energy Environ. Sci.* **2015**, 8, 2250; b)S. Park, S. W. Heo, W. Lee, D. Inoue, Z. Jiang, K. Yu, H. Jinno, D. Hashizume, M. Sekino, T. Yokota, K. Fukuda, K. Tajima, T. Someya, *Nature* **2018**, 561, 516; c)S. A. Hashemi, S. Ramakrishna, A. G. Aberle, *Energy Environ. Sci.* **2020**, 13, 685; d)B. Tian, X. Zheng, T. J. Kempa, Y. Fang, N. Yu, G. Yu, J. Huang, C. M. Lieber, *Nature* **2007**, 449, 885; e)A. M. Zamarayeva, A. E. Ostfeld, M. Wang, J. K. Duey, I. Deckman, B. P. Lechene, G. Davies, D. A. Steingart, A. C. Arias, *Sci. Adv.* **2017**, 3, e1602051; f)Y. Fang, J. Tong, Q. Zhong, Q. Chen, J. Zhou, Q. Luo, Y. Zhou, Z. Wang, B. Hu, *Nano Energy* **2015**, 16, 301; g)Y. Liu, N. Sun, J. Liu,

Z. Wen, X. Sun, S. T. Lee, B. Sun, *ACS Nano* **2018**, 12, 2893; h)T. G. Yun, D. Kim, Y. H. Kim, M. Park, S. Hyun, S. M. Han, *Adv. Mater* **2017**, 29; i)S. Qin, Q. Zhang, X. Yang, M. Liu, Q. Sun, Z. L. Wang, *Adv. Energy Mater* **2018**, 8, 1800069; j)H. Ling, J. Wu, F. Su, Y. Tian, Y. J. Liu, *Nat. Commun.* **2021**, 12, 1010; k)J. Wang, X. Li, Y. Zi, S. Wang, Z. Li, L. Zheng, F. Yi, S. Li, Z. L. Wang, *Adv. Mater* **2015**, 27, 4830; l)Z. Tian, X. Tong, G. Sheng, Y. Shao, L. Yu, V. Tung, J. Sun, R. B. Kaner, Z. Liu, *Nat. Commun.* **2019**, 10, 4913; m)R. Liu, M. Takakuwa, A. Li, D. Inoue, D. Hashizume, K. Yu, S. Umezu, K. Fukuda, T. Someya, *Adv. Energy Mater* **2020**, 10, 2000523; n)Y. Zhu, L. Shu, Q. Zhang, Y. Zhu, S. Poddar, C. Wang, Z. He, Z. Fan, *EcoMat* **2021**, 3, e12117.

[7]   a)H. Yu, N. Li, N. Zhao, *Adv. Energy Mater* **2020**, 11, 2002646; b)S. Jung, J. Oh, U. J. Yang, S. M. Lee, J. Lee, M. Jeong, Y. Cho, S. Kim, J. M. Baik, C. Yang, *Nano Energy* **2020**, 77, 105271.

[8]   a)Z. Wen, M. H. Yeh, H. Guo, J. Wang, Y. Zi, W. Xu, J. Deng, L. Zhu, X. Wang, C. Hu, L. Zhu, X. Sun, Z. L. Wang, *Sci. Adv.* **2016**, 2, e1600097; b)W. Song, X. Yin, D. Liu, W. Ma, M. Zhang, X. Li, P. Cheng, C. Zhang, J. Wang, Z. L. Wang, *Nano Energy* **2019**, 65; c)A. Maitra, R. Bera, L. Halder, A. Bera, S. Paria, S. K. Karan, S. K. Si, A. De, S. Ojha, B. B. Khatua, *Renew. Sust. Energ. Rev.* **2021**, 151.

[9]   J. Huang, Z. Ren, Y. Zhang, K. Liu, H. Zhang, H. Tang, C. Yan, Z. Zheng, G. Li, *Adv. Funct. Mater* **2021**, 31, 2010172.

[10] a)Y. Cui, C. Yang, H. Yao, J. Zhu, Y. Wang, G. Jia, F. Gao, J. Hou, *Adv. Mater* **2017**, 29, 201703080; b)S. Kim, M. Jahandar, J. H. Jeong, D. C. Lim, *Curr. Altern. Energy* **2019**, 3, 3; c)H. Tang, J. Lv, K. Liu, Z. Ren, H. T. Chandran, J. Huang, Y. Zhang, H. Xia, J. I. Khan, D. Hu, C. Yan, J. Oh, S. Chen, S. Chu, P. W. K. Fong, H. Chen, Z. Xiao, C. Yang, Z. Kan, F. Laquai, S. Lu, G. Li, *Materials Today* **2022**, 10.1016/j.mattod.2022.04.005.

[11] a)H. Xia, Y. Zhang, W. Deng, K. Liu, X. Xia, C. J. Su, U. S. Jeng, M. Zhang, J. Huang, J. Huang, C. Yan, W. Y. Wong, X. Lu, W. Zhu, G. Li, *Adv. Mater* **2022**, 34, 2107659; b)J. Huang, H. Tang, C. Yan, G. Li, *Cell Rep. Phys. Sci.* **2021**, 2, 100292; c)Y. Zhang, K. Liu, J. Huang, X. Xia, J. Cao, G. Zhao, P. W. K. Fong, Y. Zhu, F. Yan, Y. Yang, X. Lu, G. Li, *Nat. Commun.* **2021**, 12, 4815; d)J. Yu, X. Liu, Z. Zhong, C. Yan, H. Liu, P. W. K. Fong, Q. Liang, X. Lu, G. Li, *Nano Energy* **2022**, 94, 106923.

[12] Z. Ren, J. Zhou, Y. Zhang, A. Ng, Q. Shen, S. H. Cheung, H. Shen, K. Li, Z. Zheng, S. K. So, A. B. Djurišić, C. Surya, *Sol. Energy Mater Sol. Cells* **2018**, 179, 36.

[13] X. Fan, B. Xu, N. Wang, J. Wang, S. Liu, H. Wang, F. Yan, *Adv. Electron. Mater* **2017**, 3, 1600471.

[14] a)Y. Cui, H. Yao, T. Zhang, L. Hong, B. Gao, K. Xian, J. Qin, J. Hou, *Adv. Mater* **2019**, 31, 1904512; b)Y. Cui, L. Hong, T. Zhang, H. Meng, H. Yan, F. Gao, J. Hou, *Joule* **2021**, 5, 1016.

[15] a)Z. Wen, Y. Yang, N. Sun, G. Li, Y. Liu, C. Chen, J. Shi, L. Xie, H. Jiang, D. Bao, Q. Zhuo, X. Sun, *Adv. Funct. Mater* **2018**, 28, 1803684; b)Z. Ren, Q. Zheng, H. Wang, H. Guo, L. Miao, J. Wan, C. Xu, S. Cheng, H. Zhang, *Nano Energy* **2020**, 67, 104243.

[16] a)Q. Jiang, C. Wu, Z. Wang, A. C. Wang, J.-H. He, Z. L. Wang, H. N. Alshareef, *Nano Energy* **2018**, 45, 266; b)A. R. Mule, B. Dudem, H. Patnam, S. A. Graham, J. S. Yu, *ACS Sustainable Chemistry & Engineering* **2019**, 7, 16450; c)M. Lee, J. Shin, S. Kim, S. Gandla, *Sensors (Basel)* **2022**, 22; d)M. Zhang, L. Xia, S. Dang, L. Shi, A. Cao, Q. Deng, C. Du, *AIP Advances* **2019**, 9, 075221.

[17] a)T. G. Yun, M. Park, D. H. Kim, D. Kim, J. Y. Cheong, J. G. Bae, S. M. Han, I. D. Kim, *ACS Nano* **2019**, 13, 3141; b)G. Cai, P. Darmawan, M. Cui, J. Wang, J. Chen, S. Magdassi, P. S. Lee, *Adv. Energy Mater* **2016**, 6, 1501882; c)S. Cong, Y. Tian, Q. Li, Z. Zhao, F. Geng, *Adv. Mater* **2014**, 26, 4260; d)P. Yang, P. Sun, Z. Chai, L. Huang, X. Cai, S. Tan, J. Song, W. Mai, *Angew. Chem., Int. Ed. Engl.* **2014**, 53, 11935; e)L. Shen, L. Du, S. Tan, Z. Zang, C. Zhao, W. Mai, *Chem. Commun.* **2016**, 52, 6296.

[18] C. Meng, C. Liu, L. Chen, C. Hu, S. Fan, *Nano Lett.* **2010**, 10, 4025.

[19] Y. Zhang, X. Guo, J. Huang, Z. Ren, H. Hu, P. Li, X. Lu, Z. Wu, T. Xiao, Y. Zhu, G. Li, Z. Zheng, *npj Flex. Electron.* **2022**, 6, 4.

[20] Y. Yu, X. Xiao, Y. Zhang, K. Li, C. Yan, X. Wei, L. Chen, H. Zhen, H. Zhou, S. Zhang, Z. Zheng, *Adv. Mater* **2016**, 28, 4926.

[21] a)D. Chen, D. Wang, Y. Yang, Q. Huang, S. Zhu, Z. Zheng, *Adv. Energy Mater* **2017**, 7, 1700890; b)W. Zhao, M. Jiang, W. Wang, S. Liu, W. Huang, Q. Zhao, *Adv. Funct. Mater* **2020**, 31, 2009136.

[22] a)K. K. Upadhyay, M. Altomare, S. Eugénio, P. Schmuki, T. M. Silva, M. F. Montemor, *Electrochim. Acta* **2017**, 232, 192; b)Z. Cong, W. Guo, Z. Guo, Y. Chen, M. Liu, T. Hou, X. Pu, W. Hu, Z. L. Wang, *ACS Nano* **2020**, 14, 5590; c)W. Guo, Z. Cong, Z. H. Guo, P. Zhang, Y. Chen, W. Hu, Z. L. Wang, X. Pu, *Adv. Funct. Mater* **2021**, 31, 2104348.

[23] J. Chen, Z. Wang, Z. Chen, S. Cong, Z. Zhao, *Nano Lett* **2020**, 20, 1915.

[24] a)J. Cho, T. Y. Yun, H. Y. Noh, S. H. Baek, M. Nam, B. Kim, H. C. Moon, D. H. Ko, *Adv. Funct. Mater* **2020**, 30, 1909601; b)H. C. Moon, T. P. Lodge, C. D. Frisbie, *Chem. Mater* **2015**, 27, 1420; c)D. G. Seo, H. C. Moon, *Adv. Funct. Mater* **2018**, 28, 1706948.

Author contributions: J.H., Z.R. and Y.Z. contributed equally to this work. J.H. and G.L. conceived the idea and supervised the work. J.H., Z.R., Y.Z. and G.L. designed the experiments. J.H. carried out the device fabrication and majority device characterization. Y.Z. carried out the fabrication of the DDE-Au electrode. Z.R. carried out the fabrication of the ECS. K. Y. and X. Y. carried out the deposition of WO_3. Q.L. carried out the SEM measurement. P.W.F., H.T., H.X. and H.Z graphed and analyzed

the data. H.T.C., Z.Z. and G.L. revised the manuscript. All authors discussed the results and commented on the manuscript.

Competing interests: The authors declare that they have no competing interests.

Data Availability Statement: The data that support the findings of this study are available from the corresponding author upon reasonable request.